Lithographically Patterned Thin Activated Carbon Films as a New Technology Platform for On-Chip Devices

Lu Wei,[†,‡] **Naoki Nitta,**[†] **and Gleb Yushin**[†,*]

[†]School of Materials Science and Engineering, Georgia Institute of Technology, Atlanta, Georgia 30332-0245, United States and [‡]School of Materials Science and Engineering, Northwestern Polytechnical University, Xi'an, Shaanxi 710072, People's Republic of China

ABSTRACT Continuous, smooth, visibly defect-free, lithographically patterned activated carbon films (ACFs) are prepared on the surface of silicon wafers. Depending on the synthesis conditions, porous ACFs can either remain attached to the initial substrate or be separated and transferred to another dense or porous substrate of interest. Tuning the activation conditions allows one to change the surface area and porosity of the produced carbon films. Here we utilize the developed thin ACF technology to produce prototypes of functional electrical double-layer capacitor devices. The synthesized thin carbon film electrodes demonstrated very high capacitance in excess of 510 F g^{-1} (>390 F cm^{-3}) at a slow cyclic voltammetry scan rate of 1 mV s^{-1} and in excess of 325 F g^{-1} (>250 F cm^{-3}) in charge–discharge tests at an ultrahigh current density of 45 000 mA g^{-1}. Good stability was demonstrated after 10 000 galvanostatic charge–discharge cycles. The high values of the specific and volumetric capacitances of the selected ACF electrodes as well as the capacity retention at high current densities demonstrated great potential of the proposed technology for the fabrication of various on-chip devices, such as micro-electrochemical capacitors.

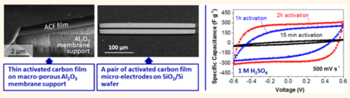

KEYWORDS: electrodes · on-chip · supercapacitors · ultracapacitors · double layer

The development of miniaturized electronic devices, such as micro-electromechanical systems, sensors, microrobots, and implantable medical devices has increased the demand for new materials processable to lithographically patternable thin films. Conventional techniques commonly utilized for semiconductor thin film processing, such as chemical and physical vapor deposition (CVD and PVD), atomic layer deposition (ALD), and sputtering, produce materials with no internal porosity. Conductive porous high surface area materials, however, are highly desired for applications in sensors[1] and micropower energy storage devices, which can be integrated on the same semiconductor chips.[2] Several promising approaches have been explored to address this demand.

CVD deposition of carbon nanotubes (CNTs),[3,4] graphene,[5] and metal nanowires[6] allow for the formation of conductive electrodes with pores in the range 20–500 nm. Patterned electrodeposition of metals and polymers,[7,8] selective etching of certain metals from metal alloys,[9] electrophoretic deposition of CNTs,[10,11] carbon onions,[12] and other nanoparticles,[13,14] layer-by-layer deposition of nanoparticles,[15,16] inkjet printing,[17] and the use of tobacco viruses as electroless deposition templates[18] offer interesting routes for the formation of porous films with pores in the range 5–200 nm. Some of these methods, however, suffer from high equipment cost, slow deposition rate, undesirably very high roughness of the produced films, and relatively broad pore size distribution.

In contrast, formation of patterned defect-free electrically conductive films with high surface area and pores in the 0.5–5 nm range has received very limited attention. Such materials, however, could offer new capabilities to a variety of on-chip devices, including various sensors, analytical tools, and energy storage devices. For example, by substituting powder-filled macroscopic columns in gas, column, and liquid chromatographies with defect-free strips of microporous media (hermetically sealed on the sides), it may offer revolutionary improvements in the detection limit and the resolution of on-chip

* Address correspondence to yushin@gatech.edu.

Received for review July 25, 2012 and accepted July 1, 2013.

Published online July 01, 2013
10.1021/nn4028129

©2013 American Chemical Society

chromatographic devices by adding the molecular sieving effect.[19] In addition, by eliminating macropores and thus forcing the molecular diffusion though the micro- and mesopores only, a dramatic enhancement of the transport rate differences may be expected.[20] Other types of sensors are based on the changes in the electrical conductivities, mechanical properties, or electrochemical response of a porous (often conductive) electrode upon analyte adsorption on (or reaction with) the active sensor surface.[4,21,22] When such sensors are based on meso- or macroporous high surface area electrodes, the use of these analytical techniques commonly suffers from limited specificity of the response. However, by offering an additional ability to further distinguish the molecules of interest, such as sieving the molecules transported to the sensor electrode by a molecular sieving layer or by adding the sieving capability to the sensor electrode itself, the degree of nonspecificity will be dramatically reduced. Finally, the majority of on-chip devices require energy storage systems to power them. Compared with microbatteries, carbon-based microelectrical double layer capacitors (micro-EDLCs) may offer several advantages, such as long cycle lifetime, broad temperature range of operation, and higher power density. The low power density of microbatteries is often insufficient for many important applications.[12,16,17,23−28] While nonporous carbon nanoparticle-based micro-EDLCs offer very high rate capabilities,[12] they exhibit limited volumetric energy storage and often poor uniformity of the electrodes.

In spite of the many promising attributes of the microporous carbon film technology, there are currently no reports on the successful fabrication of patterned microporous carbon films. Two recent studies reported formation of micrometer-thick films of microporous titanium carbide derived carbon (CDC) on ceramic and glassy carbon substrates, showed schematics of possible microfabrication routes,[23,29] but so far failed to demonstrate them. Formation of cracks and defects within CDC and poor adhesion to the substrates could be among the challenges faced by the researchers. Other limitations of the CDC technology include high equipment cost and slow fabrication process in combination with the need to use a highly corrosive chlorine gas (Cl_2).

Here we report for the first time a simple, low-cost technology to produce continuous, smooth, visibly defect-free, lithographically patterned micro/mesoporous carbon films. We utilized a natural low-cost organic compound, sucrose, as a carbon precursor. Tuning the activation conditions allows one to change the surface area and porosity of the produced carbon film. In our proof-of-concept studies, we utilized the developed porous carbon thin film technology to produce prototypes of functional EDLC devices.

RESULTS AND DISCUSSION

Well-developed fabrication routes of activated carbon (AC) powders allow high surface area and tunable pore size distribution and surface chemistry to be achieved.[19,20,30,31] Many of these routes, however, are not easily applicable for synthesis of thin activated carbon films (ACFs). Several challenges need to be overcome. First, upon heating and carbonization, the majority of polymers shrink. This leads to the formation of cracks in the carbon film (Figure S1a, Supporting Information) in the case when the adhesion between the film and the substrate is relatively stronger, or, alternatively, delaminating and forming rolls of porous carbon film (Figure S1b,c) in the case when the adhesion is relatively weaker. Second, even if a polymer does not shrink during carbonization, the interface between the polymer and the substrate must be sufficiently strong to survive stresses occurring during the synthesis. Some of such stresses are caused by cooling from carbonization or activation temperatures due to the difference in the thermal expansion coefficients between the film and the substrate. Other stresses can be caused by the capillary action of the solvent evaporating during a photoresist removal, a critical step involved in the application of the standard photolithographical technique.

We have discovered that catalyst-assisted low-temperature carbonization of an organic compound solution is an effective way to minimize some of the interface stresses described above. We further identified sucrose solution to be a well-suited carbon precursor for our project, and extensive acid-assisted cleaning and hydroxylating the wafer surface in a piranha solution was found to be a necessary step for achieving the high interface quality and continuous film formation. The precursor solution composed of sucrose and sulfuric acid (H_2SO_4) catalyst in deionized (DI) water was spin-casted on a silicon (Si) wafer, having an insulative silicon dioxide (SiO_2) layer on the surface, and dried at room temperature. By changing the solution viscosity (water content) and rotational speed of the coater, film thickness could be controlled (Figure S2). Alternatively, film thickness can be increased by the repetition of the coating/drying procedures multiple times. The final steps of continuous porous carbon film formation (Figure 1)

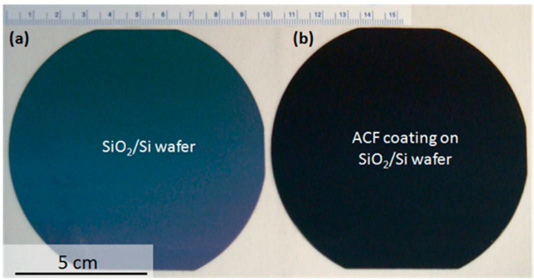

Figure 1. Optical images of the silicon wafer before and after coating with a porous activated carbon film.

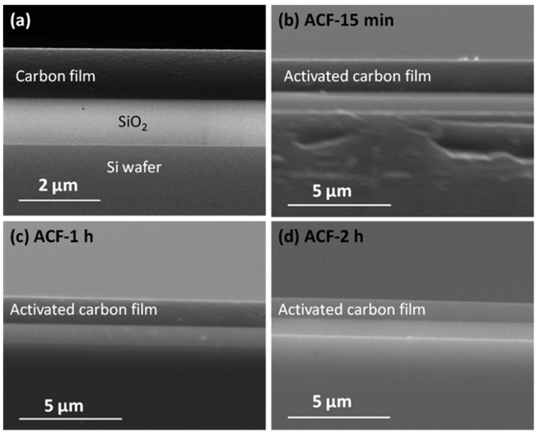

Figure 2. Cross-section SEM micrographs of the silicon wafers coated with carbon films after 700 °C carbonization (a) without following activation and with physical activation in CO_2 at 900 °C for (b) 15 min, (c) 1 h, and (d) 2 h.

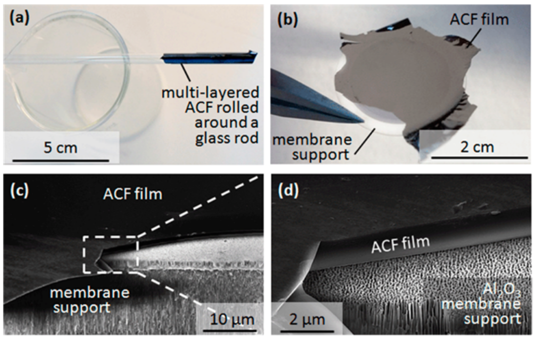

Figure 3. ACF redeposited on various substrates. Optical images of ACF on (a) a glass rod and (b) an alumina membrane. (c, d) SEM micrographs of the cleaved membrane based on ACF deposited onto anodic alumina.

include annealing at elevated temperatures to remove decomposition products of the carbohydrate and catalyst (such as H_2SO_4) residues, followed by activation. We utilized a simple physical activation process for our proof-of-concept studies, which involved annealing the produced samples at 900 °C in carbon dioxide (CO_2) to induce interconnected open porosity within carbon (Figure 2).

Before and after physical activation the sucrose-derived porous carbon films on the wafers were continuous and very uniform, with no microcracks present (Figures 1 and 2). With the activation time increasing from 15 min to 2 h, the thickness of the activated carbon films decreased from ~1.8 μm to ~1.5 μm. This can be related to both a compaction of the carbon film and a surface oxidation, a known drawback of physical activation procedures, which preferentially oxidize carbon at the surface, where higher concentration of an oxidant (such as CO_2) is present.

The produced ACFs can be separated from the substrate after prolonged soaking in solvents, such as acetone. Even being only 1–2 μm thick, they retain mechanical integrity and can be bent to a significant degree without failure. This film can also be cut or torn, transferred, and redeposited on a variety of substrates, including tubular (Figure 3a) or porous planar structures, such as alumina membrane (Figure 3b–d). In the latter case it may be used to create a thin and defect-free molecular sieve layer on a rigid, low-flow resistance ceramic support, another highly desirable process for industry technology.[32] To the best of our knowledge, we are the first to report on the feasibility of a separate micrometer-thick porous film preparation followed by film transfer technology to be applied to design such a membrane architecture.

Alternatively, by annealing the ACFs in argon gas (Ar) at 1100 °C, their adhesion to a SiO_2/Si wafer becomes sufficiently strong to survive lithographical patterning. Prior studies indicate formation of covalent bonds between Si and C at such a high temperature,[33−36] which likely explains the enhanced bonding strength.

The separation of AC films from the substrates can also be utilized to measure their mass, density, and other specific (mass-normalized) properties much more precisely than on a substrate (since the mass of the substrate contributes to the majority of the total mass). We used such stand-alone films for precise determinations of their mass-normalized gas sorption and energy storage characteristics.

The N_2 adsorption/desorption isotherm analyses at 77 K reveal the influence of activation time on the porosity development (Figure 4). The sucrose solution-derived carbon film without CO_2 activation (CF-no activation) and the activated carbon film with only 15 min of activation (ACF-15min) exhibit type-I sorption isotherms (in the Brunauer classification) with saturation at relative pressures (P/P_0) of *ca.* 0.1 and 0.2, respectively, which is characteristic for microporous materials with a very low volume of pores of >2 nm. As the activation time increases to 1 h and then to 2 h, the pore volume doubles and the isotherms change to type-IV with a significant slope at higher relative pressures, commonly associated with capillary condensation in small mesopores.[37] Increasing the activation time from 15 min to 2 h significantly increased the total amount of N_2 adsorbed at 0.99 of the relative pressure, total ACF pore volume, and BET (Brunauer–Emmett–Teller) specific surface area (SSA), as shown in Figure 4a and Table 1. Nonetheless, sample ACF-2h (activation for 2 h) showed a high BET-SSA value of 1636 $m^2\ g^{-1}$. According to nonlocal density functional theory (NLDFT) calculations,[38] all samples contain mainly micropores (Table 1); among them CF-no activation and ACF-15min samples showed virtually no pores larger than 3 nm (Figure 4b). However, activation at longer times of 1 and 2 h led to the appearance of mesopores.

Figure 5 shows the Raman spectra of sucrose solution-derived carbon films activated for different time. A perfect graphite shows only one narrow Raman-active mode, the G-band, located at 1582 cm^{-1} and corresponding to graphite in-plane vibrations.[39−41] In our test,

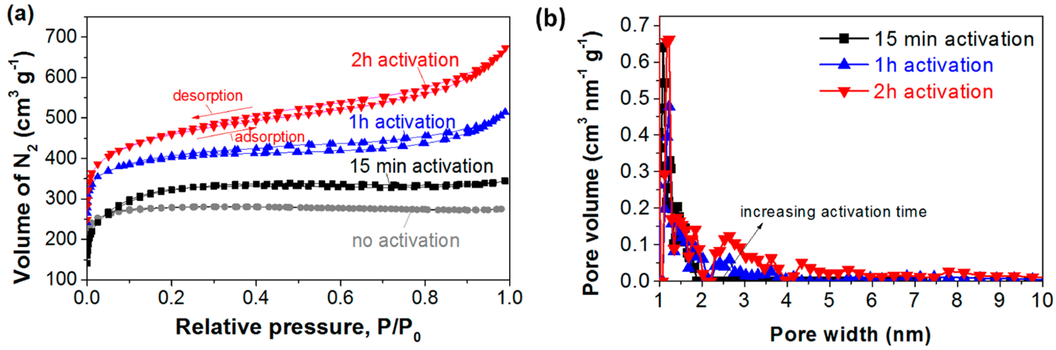

Figure 4. Porosity characterization of sucrose-derived activated carbon films: (a) N_2 adsorption/desorption isotherms; (b) pore size distribution derived from the N_2 isotherms using nonlocal density functional theory.

TABLE 1. Surface Structural Properties of Sucrose-Derived Activated Carbon Films

sample	S_{BET}[a] [m^2 g^{-1}]	total pore volume [cm^3 g^{-1}]	micropore volume (<2 nm) [cm^3 g^{-1}]
CF-no activation	989	0.35	0.35
ACF-15min	1193	0.45	0.39
ACF-1h	1435	0.65	0.46
ACF-2h	1636	0.79	0.52

[a] BET specific surface area.

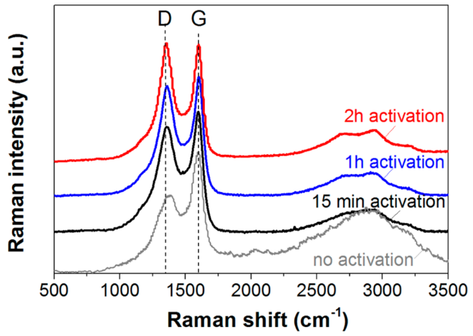

Figure 5. Raman spectra of sucrose solution-derived carbon films activated for different times.

the G-band, located at ~1600 cm^{-1}, is slightly upshifted from 1582 cm^{-1}, which is common for microporous carbons.[42,43] Disordered carbons additionally show the D-band at ~1350 cm^{-1}, which is associated with a double-resonance Raman process in disordered carbon.[41,44] The position and the width of this band may vary, depending on the structure of the disordered carbon, its uniformity, and the presence of functional groups.[45] We can see that prior to activation the integrated intensity of the D-band is smaller than that of the G-band. However, with prolonging the activation time, the relative intensity of the D-band increases, suggesting formation of multiple defects. The lack of sharp and strong peaks in the spectral range 2400−3300 cm^{-1} (2D, D+G, T+D, T+G, 2D′, and other bands) suggests the lack of graphitic ribbon structures in the samples.[41]

X-ray photoelectron spectroscopy (XPS) analysis (Figure 6) revealed high purity of the produced ACF samples with only a small atomic fraction of oxygen visible (less than 5 at. %).

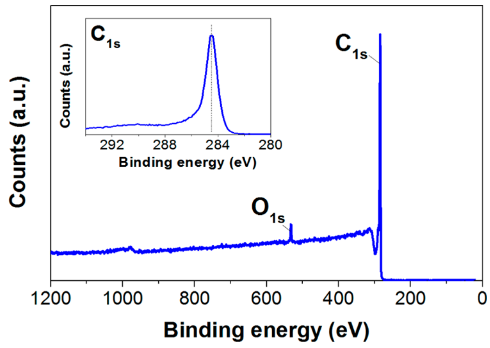

Figure 6. Typical XPS spectra of an ACF, showing a small (3 at. %) oxygen peak and strong carbon peak present. The inset shows a high-resolution C 1s spectrum with a single strong peak present. This ACF sample was activated for 1 h.

Traditional lithographical techniques have been utilized to pattern rectangular ACF electrodes on a SiO_2/Si wafer. Briefly, after activation and annealing at 1100 °C, a negative photoresist was patterned using a custom-designed mask. After an e-beam deposition of a platinum (Pt)/gold (Au) bilayer and the lift-off of the remaining photoresist, patterned Pt/Au strips of the desired electrode geometry were produced and served as a protection mask against oxygen plasma etching of the ACFs. An additional patterned layer of Pt/Au was deposited to serve as a current collector. Figure 7 shows key fabrication steps, and the Materials and Methods section provides additional details.

Figure 8 shows examples of the scanning electron microscopy (SEM) and optical microscopy micrographs of the lithographically defined rectangular ACF electrodes produced according to the process flow described by Figure 7.

Electrochemical measurements of ACF films were carried out in a two-electrode configuration with symmetric ACF film electrodes in aqueous 1 M H_2SO_4 electrolyte. Figure 9 shows the effect of activation on the shape of the cyclic voltammograms (CVs) of the ACF samples. When activated for over 1 h, ACFs show a good response with a rectangular shape and no

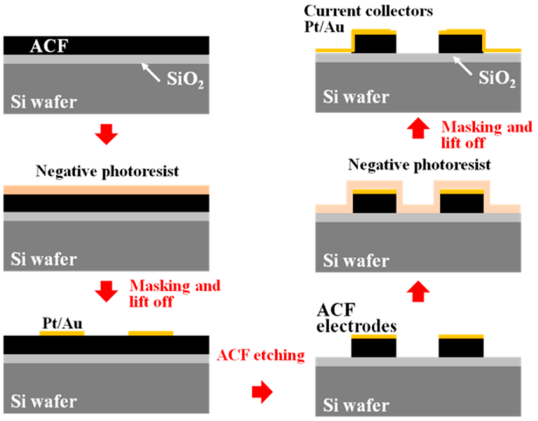

Figure 7. Schematic of the fabrication of ACF electrodes integrated onto a silicon wafer.

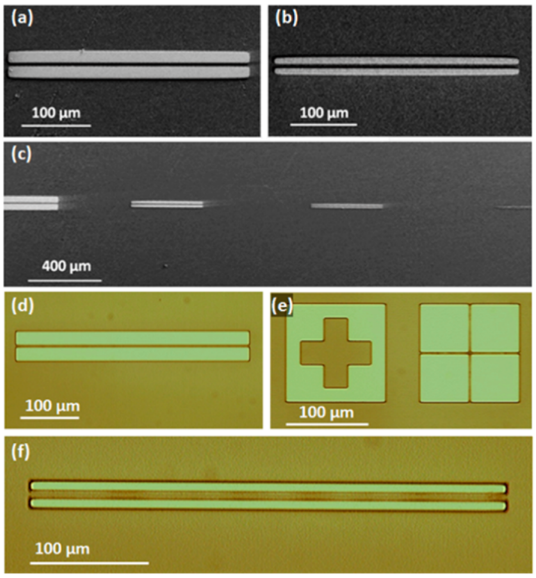

Figure 8. ACF electrodes lithographically patterned according to the process flow described above: (a–c) SEM micrographs showing a top view of selected ACF electrodes of different dimensions, (d, f) optical micrographs showing a top view of selected ACF electrodes, and (e) alignment marks. Oxidative etching in oxygen plasma was utilized for C etching.

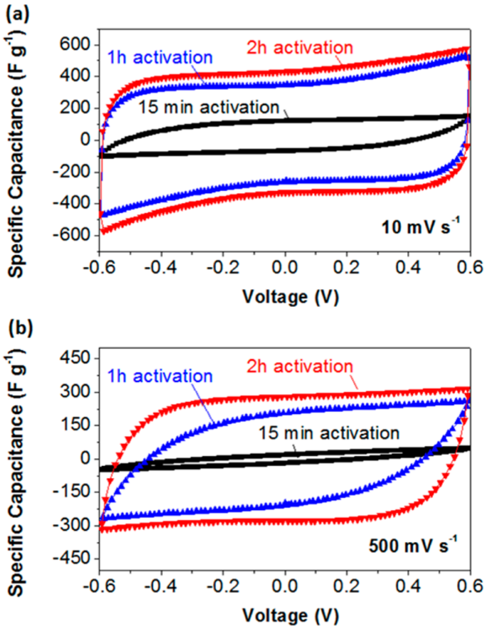

Figure 9. Cyclic voltammograms of ACFs in symmetric two-electrode cells with 1 M H_2SO_4 electrolyte recorded at (a) 10 mV s^{-1} and (b) 500 mV s^{-1}.

evident Faradaic peaks visible, which is characteristic of a nearly ideal EDLC. A short activation time (15 min), however, does not provide sufficiently rapid electrolyte access to the internal porosity of the ACF electrode. This sample (ACF-15min) showed relatively small specific capacitance and significantly distorted shape of the CV, particularly at fast (500 mV s^{-1}) scan rates (Figure 9b). Figure 10 summarizes the impact of the activation conditions on the specific gravimetric (Figure 10a) and volumetric (Figure 10b) capacitance retention at increasing sweep rates. The average specific capacitance of the ACF produced during 2 h activation (ACF-2h sample) decreases by 36% from 514 F g^{-1} to 330 F g^{-1} when the sweep rate increases from 1 mV s^{-1} to 100 mV s^{-1}. In contrast, the capacitance decrease of the ACF-15min sample is significantly more pronounced, reaching nearly 87%, from 142 F g^{-1} to 19 F g^{-1} at identical conditions. The poor electrochemical performance of ACF-15min cannot be explained only by its low surface area and low pore volume (Table 1). The existence of bottleneck pores in ACF-15min limiting the ion transport at fast scan rates[46] is a more probable explanation. The results of the electrochemical impedance spectroscopy measurements also revealed significantly faster frequency response of the EDLCs based on ACF exposed to longer activation time (Figure 10c). The capacitance of ACF activated for 15 min (ACF-15min) does not show signs of saturation at a frequency as low as 0.01 Hz, suggesting that tortuous diffusion paths for electrolyte ions prevent the achievement of the equilibrium ion adsorption. Increasing activation time to 1 h and then to 2 h results in a major improvement in the frequency response, by more than an order of magnitude. Comparing the frequencies at which capacitance drops to 50% of its maximum value ($f_{0.5}$), we clearly see that the sample ACF-2h demonstrates the fastest frequency response with $f_{0.5}$ = 0.9 Hz. The enlarged pore size (Figure 4b) combined with the proposed elimination of bottleneck pores in ACFs and the absence of obstacles for ion diffusion induced by the prolonged activation time are likely responsible for the observed phenomenon.

The volumetric capacitance of the produced ACF micro-EDLC electrodes exceeds that of the majority of the prior art studies of micro-EDLC electrodes by more than an order of magnitude. For example, Pech *et al.* fabricated micro-supercapacitors prepared using

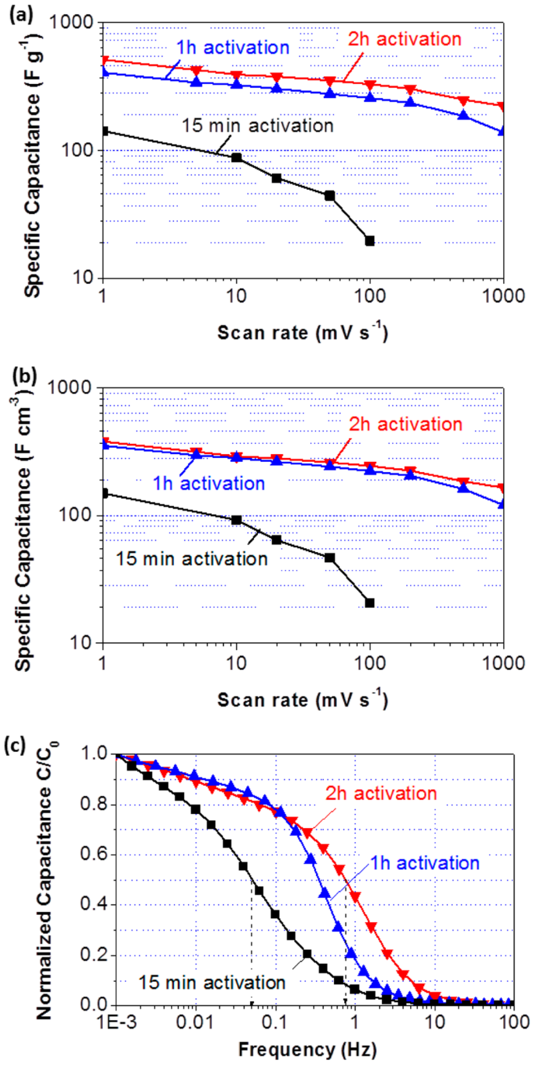

Figure 10. Rate performance of symmetric ACF electrode cells in 1 M H_2SO_4 electrolyte: (a) gravimetric and (b) volumetric capacitance of ACFs as a function of CV scan rate and (c) frequency response.

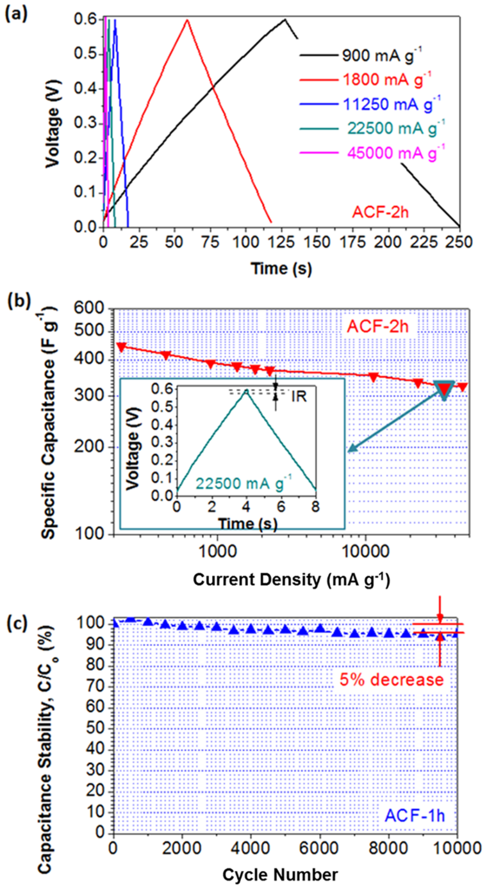

Figure 11. Charge–discharge characteristics of symmetric ACF electrode cells in 1 M H_2SO_4 electrolyte: (a) C–D curves and (b) capacitance as a function of current density of a cell based on 2 h activated ACF electrodes for current densities up to 45 000 mA g^{-1}; (c) cycle stability of a cell based on 1 h activated ACF electrodes tested at current densities of ∼10 000 mA g^{-1}. The inset in (b) shows a low *IR* drop of the electrode at a very high current density of 22 500 mA g^{-1}.

inkjet printing technology showed the estimated volumetric capacitance between 1.6 and 2.7 F cm^{-3}. They also produced a micro-supercapacitor with AC powder electrodes by electrophoretic deposition technique,[12] which has a stack capacitance of just 9.0 F cm^{-3}. In contrast, ACF micro-EDLC electrodes exhibited volumetric capacitances in excess of 250 F cm^{-3} due to high gravimetric capacity and the absence of pores, inevitable between individual AC or nanosize carbon particles utilized in the prior art studies.

The high values of the specific and area-normalized capacitance (up to 514 F g^{-1} and 27 μF cm^{-2}, respectively) exhibited by ACF samples were somewhat surprising. The powder AC samples generally exhibit specific capacitance in the range from 120 to 200 F g^{-1} in aqueous electrolytes, with only a few studies reporting capacitances in excess of 250 F g^{-1}.[47] One possible explanation is an excellent electrical connectivity within ACF combined with full accessibility of the internal surface to electrolyte ions, which may allow the ACF capacitance to more closely approach a value of ∼70 μF cm^{-2} reported for the edge plane of graphite. Indeed, in contrast with 100–200 μm thick powder-based electrodes, which have high-resistance point-contacts between individual particles and suffer from the additional electrical resistance caused by electrically isolative polymer binder present within the electrode, the binder-free 1–2 μm thin ACF electrodes should exhibit several orders of magnitude lower resistance. Similarly, conventional AC electrodes have a broad pore size distribution with some of the small sub-nanometer pores being not fully accessible for ion electroadsorption.[49,50] In the case of ACF, a large portion of the pores have dimensions larger than 1 nm in size and, therefore, both sides of the pore walls should be accessible to electrolyte ions. We recognize, however, that sub-nanometer pores may allow distortion of the solvation shells and lead to closer approach of ions to the pore walls, which may enhance the specific capacitance, as proposed in 2006 in microporous carbon electrodes in organic electrolytes.[51] ACFs do not have such small pores. However, the defects in the carbon structure and edge planes of graphene segments may also cause solvation shell distortion and thus similarly lead to high normalized capacitance.[52,53]

A small fraction of oxygen detected in ACF samples by X-ray photoelectron spectrometer studies (Figure 6) may be present within functional groups, which may contribute to the pseudocapacitive (reversible reduction–oxidation) reactions between the ACF and aqueous electrolyte. Such reactions may cause degradation of the EDLC during cycling and potentially contribute to self-discharge, which would reveal itself as a constant slope of the CV curves. However, the small amount of the detected oxygen (less than 5 at. %, in Figure 6 and likely could be further reduced by annealing the samples in Ar gas prior to XPS measurements) and virtually no significant constant slope seen in our CV tests (Figure 9) suggested a rather small contribution of redox reactions and small self-discharge rate, both being comparable to that observed in commercial activated carbon powders. The performance of supercapacitors in real applications is primarily determined by their charge–discharge (C–D) characteristics, which reveal their energy and power performance. The shape of the C–D curves in ACF electrodes is linear (Figure 11a), as expected for nearly ideal capacitors. The highest specific capacitance and the best capacity retention were achieved in the ACF-2h electrode. A specific capacitance in excess of 325 F g^{-1} was observed at a very high current density of 45 000 mA g^{-1}, which has never been reported before for any type of EDLC or supercapacitor electrodes.[30,31,42,46,48,49,54–57] The large average pore size of ACF-2h (Figure 4b) may have assisted in the low resistance to the transport of ions within this sample. Indeed, at a current density of 22 500 mA g^{-1} the IR drop is only 5% of the total voltage range (inset in Figure 11b). After 10 000 C–D cycles at a current density of ~10 000 mA g^{-1} the sample ACF-1h showed the highest degradation of 5% (Figure 11c), which is quite modest for carbon electrodes in acidic electrolytes.

CONCLUSIONS

The demonstrated ability to produce patterned ACFs and tune electrochemical characteristics of ACF electrodes suggests that the proposed technology could be applicable for the fabrication of various on-chip devices, such as micro-electrochemical capacitors (micro-supercapacitors). The values of the specific and volumetric capacitances of the selected ACF electrodes in combination with the capacity retention at high current densities are unprecedented. The ability to transfer thin ACFs to macroporous substrates may additionally open the door to the fabrication of high-throughput, high-pressure/low-resistance filters and membranes for gas and liquid separation. Fabrication and performance characterization of such devices will be reported elsewhere.

MATERIALS AND METHODS

Activated Carbon Film Preparation. Sucrose, DI water, and H_2SO_4 were mixed with a mass fraction of 1:0.5:0.1 to form an aqueous sucrose/catalyst solution. The solution was uniformly distributed onto a 10 cm diameter Si wafer with a 1 μm SiO_2 coating (the Si wafer was pre-etched in piranha solution in order to hydroxylate the surface of the Si wafer, making it extremely hydrophilic) by using a CEE 100CB spinner (Brewer Science, Inc., USA) at a spin speed of 800 rpm for 30 s. In order to increase the thickness of the sucrose solution coating, application of sucrose solution by spin coating was repeated. Next, the sucrose solution coating was carbonized and annealed in a vacuum furnace (Across International, USA) at 700 °C for 2 h at a heating rate of 4 °C min^{-1}. After carbonization and annealing, the Si wafer with carbon coating was subsequently heated to 900 °C under an Ar flow and then activated using a pure CO_2 gas (99.9%, Air Gas, USA) flowing at a rate of 500 mL min^{-1} for 15 min to 2 h. The samples were then cooled slowly under an Ar flow. The activated carbon film samples are tagged as ACF-15min, ACF-1h, and ACF-2h, referring to different activation times.

Activated Carbon Film Characterization. The thickness and morphology of the prepared carbon films was observed by a Leo 1530 (LEO, Osaka, Japan, now Nano Technology Systems Division of Carl Zeiss SMT, USA) scanning electron microscope. Before analyzing the surface and pore characterization, the activated carbon films were peeled off from the Si wafers by immersing them in organic solution and were degassed at 300 °C using the VacPrep 061 degasser (Micromeritics Instrument Corporation, USA) to remove moisture and other adsorbed contaminants. After that, the carbon films were characterized by N_2 adsorption/desorption measurements at −196 °C using a TriStar II 3020 surface area and porosity analyzer (Micromeritics Instrument Corporation, USA). The SSAs (S_{BET}) were calculated from N_2 adsorption isotherms using the Brunauer–Emmett–Teller equation in the range of relative pressures from 0.1 to 0.3. Porosity distributions were calculated by the nonlocal density functional theory analysis of N_2 adsorption in carbon slit pores. The Raman spectra were recorded using a Horiva (LabRam HR-800) spectrometer. The source of radiation was a laser operating at a wavelength of 514 nm and a power of 25 mW. XPS analysis was done using the Thermo K-Alpha (Al Kα peak).

Fabrication of On-Chip Microactivated Carbon Film Electrodes. The process flow for the fabrication of a micro-EDLC with ACF electrodes on a Si wafer is shown in Figure 7. In order to increase the interface adhesion between the ACF and the SiO_2 insulating layer, the Si wafer with ACF coating was first heat treated at 1100 °C under Ar flow for 1.5 h. After that, standard photolithography techniques were used for patterning ACF capacitor electrodes. First, negative resist NR9-1500PY (Futurrex, Inc., USA) was spin coated on the surface of the ACF coating at a speed of 800 rpm for 40 s. Then the spin-coated photoresist was baked for 60 s at 150 °C on a hot plate. The baked photoresist was patterned from a mask with a UV exposure (Karl Suss MA-6 mask aligner). Postexposure bake was done for 60 s at 100 °C on a hot plate. Then the sample was developed in the RD6 developer. After photoresist rinsing in DI water and drying, thin Pt (50 nm)/Au (50 nm) coatings were deposited on the surface; later, the photoresist was lifted off in acetone. The unwanted ACF was etched in oxygen plasma; then, the parallel column-like ACF electrodes were formed on the Si wafer. Next, another photolithography process was employed using the same procedures but different mask to get Pt (100 nm)/Au (100 nm) current collectors on the surface of ACF electrodes.

EDLCs with Activated Carbon Film Electrodes. Before assembling EDLC cells, the ACFs were placed in a vacuum oven (100 °C) overnight to remove moisture and residual hydrocarbons. In order to reduce potential errors in estimating the weight of the samples, the presented electrochemical measurements were performed on ACF samples separated from the wafers and cut into sizes of 1 cm^2 or larger for EDLC electrodes. Sandwich-type electrochemical cells were set up in a glass beaker with two symmetrical carbon film electrodes separated by two 25 μm GORE PTFE separators. Gold foil (Alfa Aesar, USA) was attached to each electrode and served as current collectors. A 1 M H_2SO_4 solution was used as the electrolyte. Cyclic voltammetry studies were performed using a Solartron 1480A MultiStat (Solartron Analytical, UK) in the voltage range -0.6 to $+0.6$ V and in scan rates from 1 to 1000 mV s^{-1}. Electrochemical impedance spectroscopy measurements were carried out using a Gamry Reference 600 potentiostat/galvanostat/ZRA (Gamry Instruments, Inc., USA) in the frequency range 1 mHz to 100 kHz with a 10 mV ac amplitude. Galvanostatic charge−discharge cycle tests were measured using an Arbin BT-2000 testing system (Arbin Instruments, USA) in the voltage range 0−0.6 V and at charge−discharge current densities between 100 and 45 000 mA g^{-1}, based on the mass of a single electrode.

Conflict of Interest: The authors declare no competing financial interest.

Supporting Information Available: Additional figures. This material is available free of charge *via* the Internet at http://pubs.acs.org.

Acknowledgment. This work was partially supported by the gift from Semiconductor Research Corporation.

REFERENCES AND NOTES

1. Schedin, F.; Geim, A. K.; Morozov, S. V.; Hill, E. W.; Blake, P.; Katsnelson, M. I.; Novoselov, K. S. Detection of Individual Gas Molecules Adsorbed on Graphene. *Nat. Mater.* **2007**, *6*, 652–655.
2. Beidaghi, M.; Wang, C. L. On-Chip Micro-Power: Three Dimensional Structures for Micro-Batteries and Micro-Supercapacitors. In *Micro- and Nanotechnology Sensors, Systems, and Applications II*; George, T.; Islam, M. S.; Dutta, A. K., Eds.; Proceedings of SPIE: Orlando, FL, United States, 2010.
3. Evanoff, K.; Khan, J.; Balandin, A. A.; Magasinski, A.; Ready, W. J.; Fuller, T. F.; Yushin, G. Towards Ultrathick Battery Electrodes: Aligned Carbon Nanotube-Enabled Architecture. *Adv. Mater.* **2012**, *24*, 533–537.
4. Baughman, R. H.; Zakhidov, A. A.; Heer, W. A. d. Carbon Nanotubes-the Route toward Applications. *Science* **2002**, *297*, 787–792.
5. Miller, J. R.; Outlaw, R. A.; Holloway, B. C. Graphene Double-Layer Capacitor with AC Line-Filtering Performance. *Science* **2010**, *329*, 1637–1639.
6. Benson, J.; Boukhalfa, S.; Magasinski, A.; Kvit, A.; Yushin, G. Chemical Vapor Deposition of Aluminum Nanowires on Metal Substrates for Electrical Energy Storage Applications. *ACS Nano* **2012**, *6*, 118–125.
7. Taberna, L.; Mitra, S.; Poizot, P.; Simon, P.; Tarascon, J. M. High Rate Capabilities Fe_3O_4-Based Cu Nano-Architectured Electrodes for Lithium-Ion Battery Applications. *Nat. Mater.* **2006**, *5*, 567–573.
8. Ramanathan, K.; Bangar, M. A.; Yun, M. H.; Chen, W. F.; Mulchandani, A.; Myung, N. V. Individually Addressable Conducting Polymer Nanowires Array. *Nano Lett.* **2004**, *4*, 1237–1239.
9. Li, Y.; Antoniou, A. Synthesis of Transversely Isotropic Nanoporous Platinum. *Scr. Mater.* **2012**, *66*, 503–506.
10. Du, C. S.; Pan, N. High Power Density Supercapacitor Electrodes of Carbon Nanotube Films by Electrophoretic Deposition. *Nanotechnology* **2006**, *17*, 5314–5318.
11. Du, C. S.; Pan, N. Supercapacitors Using Carbon Nanotubes Films by Electrophoretic Deposition. *J. Power Sources* **2006**, *160*, 1487–1494.
12. Pech, D.; Brunet, M.; Durou, H.; Huang, P. H.; Mochalin, V.; Gogotsi, Y.; Taberna, P. L.; Simon, P. Ultrahigh-Power Micrometre-Sized Supercapacitors Based on Onion-Like Carbon. *Nat. Nanotechnol.* **2010**, *5*, 651–654.
13. Li, J.; Yang, Q. M.; Zhitomirsky, I. Composite Electrodes for Electrochemical Supercapacitors. *Nanoscale Res. Lett.* **2010**, *5*, 512–517.
14. Li, J.; Zhitomirsky, I. Cathodic Electrophoretic Deposition of Manganese Dioxide Films. *Colloids Surf., A* **2009**, *348*, 248–253.
15. Lee, S. W.; Yabuuchi, N.; Gallant, B. M.; Chen, S.; Kim, B.-S.; Hammond, P. T.; Shao-Horn, Y. High-Power Lithium Batteries from Functionalized Carbon-Nanotube Electrodes. *Nat. Nanotechnol.* **2010**, *5*, 531–537.
16. Lee, S. W.; Kim, B. S.; Chen, S.; Shao-Horn, Y.; Hammond, P. T. Layer-by-Layer Assembly of All Carbon Nanotube Ultrathin Films for Electrochemical Applications. *J. Am. Chem. Soc.* **2009**, *131*, 671–679.
17. Pech, D.; Brunet, M.; Taberna, P. L.; Simon, P.; Fabre, N.; Mesnilgrente, F.; Conedera, V.; Durou, H. Elaboration of A Microstructured Inkjet-Printed Carbon Electrochemical Capacitor. *J. Power Sources* **2010**, *195*, 1266–1269.
18. Royston, E.; Ghosh, A.; Kofinas, P.; Harris, M. T.; Culver, J. N. Self-Assembly of Virus-Structured High Surface Area Nanomaterials and Their Application as Battery Electrodes. *Langmuir* **2008**, *24*, 906–912.
19. Saufi, S. M.; Ismail, A. F. Fabrication of Carbon Membranes for Gas Separation-A Review. *Carbon* **2004**, *42*, 241–259.
20. Yang, R. T. *Adsorbents: Fundamentals and Applications*; Wiley & Sons, Inc.: Hoboken, NJ, USA, 2003.
21. Collins, P. G.; Bradley, K.; Ishigami, M.; Zettl, A. Extreme Oxygen Sensitivity of Electronic Properties of Carbon Nanotubes. *Science* **2000**, *287*, 1801–1804.
22. Comini, E.; Faglia, G.; Sberveglieri, G.; Pan, Z. W.; Wang, Z. L. Stable and Highly Sensitive Gas Sensors Based on Semiconducting Oxide Nanobelts. *Appl. Phys. Lett.* **2002**, *81*, 1869–1871.
23. Chmiola, J.; Largeot, C.; Taberna, P. L.; Simon, P.; Gogotsi, Y. Monolithic Carbide-Derived Carbon Films for Micro-Supercapacitors. *Science* **2010**, *328*, 480–483.
24. Armand, M.; Tarascon, J. M. Building Better Batteries. *Nature* **2008**, *451*, 652–657.
25. Simon, P.; Gogotsi, Y. Materials for Electrochemical Capacitors. *Nat. Mater.* **2008**, *7*, 845–854.
26. Xue, M. Q.; Xie, Z.; Zhang, L. S.; Ma, X. L.; Wu, X. L.; Guo, Y. G.; Song, W. G.; Li, Z. B.; Cao, T. B. Microfluidic Etching for Fabrication of Flexible and All-Solid-State Micro Supercapacitor Based on MnO_2 Nanoparticles. *Nanoscale* **2011**, *3*, 2703–2708.
27. Gao, W.; Singh, N.; Song, L.; Liu, Z.; Reddy, A. L. M.; Ci, L. J.; Vajtai, R.; Zhang, Q.; Wei, B. Q.; Ajayan, P. M. Direct Laser Writing of Micro-Supercapacitors on Hydrated Graphite Oxide Films. *Nat. Nanotechnol.* **2011**, *6*, 496–500.
28. Ahn, H. J.; Kim, W. B.; Seong, T. Y. $Co(OH)_2$-Combined Carbon-Nanotube Array Electrodes for High-Performance Micro-Electrochemical Capacitors. *Electrochem. Commun.* **2008**, *10*, 1284–1287.
29. Heon, M.; Lofland, S.; Applegate, J.; Nolte, R.; Cortes, E.; Hettinger, J. D.; Taberna, P. L.; Simon, P.; Huang, P. H.; Brunet, M.; Gogotsi, Y. Continuous Carbide-Derived Carbon Films with High Volumetric Capacitance. *Energ. Environ. Sci.* **2011**, *4*, 135–138.
30. Wei, L.; Sevilla, M.; Fuertesc, A. B.; Mokaya, R.; Yushin, G. Hydrothermal Carbonisation of Abundant Renewable Natural Organic Chemicals for High-Performance Supercapacitor Electrodes. *Adv. Energ. Mater.* **2011**, *1*, 356–361.
31. Wei, L.; Sevilla, M.; Fuertes, A. B.; Mokaya, R.; Yushin, G. Polypyrrole-Derived Activated Carbons for High-Performance Electrical Double-Layer Capacitors with Ionic Liquid Electrolyte. *Adv. Funct. Mater.* **2012**, *22*, 827–834.
32. Shiflett, M. B.; Foley, H. C. Ultrasonic Deposition of High-Selectivity Nanoporous Carbon Membranes. *Science* **1999**, *285*, 1902–1905.

33. Luo, J. S.; Lin, W. T. Localized Epitaxial Growth of Hexagonal and Cubic SiC Films on Si by Vacuum Annealing. *Appl. Phys. Lett.* **1996**, *69*, 916–918.
34. Yushin, G. N.; Aleksov, A.; Wolter, S. D.; Okuzumi, F.; Prater, J. T.; Sitar, Z. Wafer Bonding of Highly Oriented Diamond to Silicon. *Diam. Relat. Mater.* **2004**, *13*, 1816–1821.
35. Yushin, G. N.; Wolter, S. D.; Kvit, A. V.; Collazo, R.; Stoner, B. R.; Prater, J. T.; Sitar, Z. Study of Fusion Bonding of Diamond to Silicon for Silicon-on-Diamond Technology. *Appl. Phys. Lett.* **2002**, *81*, 3275–3277.
36. Wolter, S. D.; Yushin, G. N.; Okuzumi, F.; Stoner, B. R.; Prater, J. T.; Sitar, Z. Direct Fusion Bonding of Silicon to Polycrystalline Diamond. *Diam. Relat. Mater.* **2002**, *11*, 482–486.
37. Brunauer, S.; Emmett, P. H.; Teller, E. Adsorption of Gases in Multimolecular Layers. *J. Am. Chem. Soc.* **1938**, *60*, 309–319.
38. Ravikovitch, P. I.; Neimark, A. V. Characterization of Nanoporous Materials from Adsorption and Desorption Isotherms. *Colloids Surf., A* **2001**, *187–188*, 11–21.
39. Nemanich, R. J.; Solin, S. A. First- and Second-Order Raman Scattering from Finite-Size Crystals of Graphite. *Phys. Rev. B* **1979**, *20*, 392–401.
40. Tuinstra, F.; Koenig, J. L. Raman Spectrum of Graphite. *J. Chem. Phys.* **1970**, *53*, 1126–1131.
41. Tan, P. H.; Dimovski, S.; Gogotsi, Y. Raman Scattering of Non-Planar Graphite: Arched Edges, Polyhedral Crystals, Whiskers and Cones. *Philos. Trans. R. Soc. A* **2004**, *362*, 2289–2310.
42. Korenblit, Y.; Rose, M.; Kockrick, E.; Borchardt, L.; Kvit, A.; Kaskel, S.; Yushin, G. High-Rate Electrochemical Capacitors Based on Ordered Mesoporous Silicon Carbide-Derived Carbon. *ACS Nano* **2010**, *4*, 1337–1344.
43. Yushin, G. N.; Hoffman, E. N.; Nikitin, A.; Ye, H.; Barsoum, M. W.; Gogotsi, Y. Synthesis of Nanoporous Carbide-Derived Carbon by Chlorination of Titanium Silicon Carbide. *Carbon* **2005**, *43*, 2075–2082.
44. Thomsen, C.; Reich, S. Double Resonant Raman Scattering in Graphite. *Phys. Rev. Lett.* **2000**, *85*, 5214–5217.
45. Ferrari, A. C.; Robertson, J. Raman Spectroscopy of Amorphous, Nanostructured, Diamond-Like Carbon, and Nanodiamond. *Philos. Trans. R. Soc. A* **2004**, *362*, 2477–2512.
46. Kajdos, A.; Kvit, A.; Jones, F.; Jagiello, J.; Yushin, G. Tailoring the Pore Alignment for Rapid Ion Transport in Microporous Carbons. *J. Am. Chem. Soc.* **2010**, *132*, 3252–3253.
47. Wei, L.; Yushin, G. Nanostructured Activated Carbons from Natural Precursors for Electrical Double Layer Capacitors. *Nano Energy* **2012**, *1*, 552–565.
48. Frackowiak, E. Carbon Materials for Supercapacitor Application. *Phys. Chem. Phys.* **2007**, *9*, 1774–1785.
49. Korenblit, Y.; Kajdos, A.; West, W. C.; Smart, M. C.; Brandon, E. J.; Kvit, A.; Jagiello, J.; Yushin, G. *In Situ* Studies of Ion Transport in Microporous Supercapacitor Electrodes at Ultralow Temperatures. *Adv. Funct. Mater.* **2012**, *22*, 1655–1662.
50. Wei, L.; Yushin, G. Electrical Double Layer Capacitors with Activated Sucrose-Derived Carbon Electrodes. *Carbon* **2011**, *49*, 4830–4838.
51. Chmiola, J.; Yushin, G.; Gogotsi, Y.; Portet, C.; Simon, P. Anomalous Increase in Carbon Capacitance at Pore Size below 1 nm. *Science* **2006**, *313*, 1760–1763.
52. Portet, C.; Yushin, G.; Gogotsi, Y. Electrochemical Performance of Carbon Onions, Nanodiamonds, Carbon Black and Multiwalled Nanotubes in Electrical Double Layer Capacitors. *Carbon* **2007**, *45*, 2511–2518.
53. Gallagher, K. G.; Yushin, G.; Fuller, T. F. The Role of Nanostructure in the Electrochemical Oxidation of Model-Carbon Materials in Acidic Environments. *J. Electrochem. Soc.* **2010**, *157*, B820–B830.
54. Presser, V.; Zhang, L. F.; Niu, J. J.; McDonough, J.; Perez, C.; Fong, H.; Gogotsi, Y. Flexible Nano-Felts of Carbide-Derived Carbon with Ultra-High Power Handling Capability. *Adv. Energ. Mater.* **2011**, *1*, 423–430.
55. Kurig, H.; Jänes, A.; Lust, E. Electrochemical Characteristics of Carbide-Derived Carbon|1-Ethyl-3-Methylimidazolium Tetrafluoroborate Supercapacitor Cells. *J. Electrochem. Soc.* **2010**, *157*, A272–A279.
56. Jänes, A.; Lust, E. Electrochemical Characteristics of Nanoporous Carbide-Derived Carbon Materials in Various Nonaqueous Electrolyte Solutions. *J. Electrochem. Soc.* **2006**, *153*, A113–A116.
57. Kovalenko, I.; Bucknall, D.; Yushin, G. Detonation Nanodiamond and Onion-Like Carbon-Embedded Polyaniline for Supercapacitors. *Adv. Funct. Mater.* **2010**, *20*, 3979–3986.